Dalton Transactions

Lithium Selenometallates of Triel Elements, Li5MSe4 (M = Al and Ga), Aliovalent Doping and Their Ionic Conductivity

Journal:	*Dalton Transactions*
Manuscript ID	DT-ART-08-2022-002843.R1
Article Type:	Paper
Date Submitted by the Author:	26-Oct-2022
Complete List of Authors:	Sundaramoorthy, Santhoshkumar; Missouri University of Science and Technology, Chemistry Chernatynskiy, Aleksandr; Missouri University of Science and Technology, Physics Gerasimchuk, Nikolay; Missouri State University, Department of Chemistry Choudhury, Amitava; Missouri University of Science and Technology, Chemistry

ARTICLE

Lithium Selenometallates of Triel Elements, Li_5MSe_4 (M = Al and Ga), Aliovalent Doping and Their Ionic Conductivity

Santhoshkumar Sundaramoorthy,[a] Aleksandr V. Chernatynskiy,[b] Nikolay Gerasimchuk,[c] and Amitava Choudhury[a,*]

Received 00th January 20xx,
Accepted 00th January 20xx

DOI: 10.1039/x0xx00000x

Ternary selenometallates, Li_5MSe_4 (*M* = Al (**I**) and Ga (**II**)) have been synthesized for the first time through high temperature solid-state reactions combining elements and Li_2Se in stochiometric composition. Li_5MSe_4 crystallizes in $P2_1/m$ space group, forming a pseudo 2-D layer type structure with edge sharing $LiSe_4$ and MSe_4 tetrahedra along the *a*-axis. These layers are interleaved by octahedrally coordinated Li ions located in the interlayer space. AC impedance spectroscopy measurements yield a room temperature ionic conductivity of 0.60 x 10^{-7} and 0.58 x 10^{-7} S cm^{-1} with calculated activation energies of 0.51 and 0.48 eV for **I** and **II**, respectively. An aliovalent substitution of Sn^{4+} in Li_5MSe_4 yields compositions of $Li_{4.66}Al_{0.82}Sn_{0.22}Se_4$ (**III**) and $Li_{4.37}Ga_{0.89}Sn_{0.24}Se_4$ (**IV**), which crystallize in $P2_1/m$ and $P\bar{3}m1$ space groups, respectively. Sn-doped samples show ~5 fold increase in ionic conductivity, 3.37 x 10^{-7} S cm^{-1} and 2.4 x 10^{-7} S cm^{-1} with an activation energy of 0.54 and 0.28 eV, respectively, for **III** and **IV**. The optical band gap values of the compounds are 3.65 and 3.2 eV for **I** and **II**, respectively, as measured by diffuse reflectance spectroscopy. Density Function Theory (DFT) calculations predict major contribution from Se 4*p*-states in forming the top of valence band and strongly hybridized Se 4*p* and n*s* orbital of Al and Ga forming the bottom of the conduction band with almost no contribution from the Li *s*-states near the Fermi level indicating their ionic interactions with the ligand.

Introduction

Ternary and quaternary chalcogenides with aliovalent substitutions are widely explored in search for superionic conductors for all-solid-state Li-ion batteries (LIBs).[1] The replacement of flammable liquid electrolyte with solid superionic conductors can increase the safety as well as the energy density of solid-state batteries.[2] Among various superionic conductors, chalcogenides show a superior performance in terms of high ionic conductivity and low activation barrier owing to weak interactions between Li ions and highly polarizable chalcogenide lattice.[3] On the other hand, the oxide-based solid electrolytes such as LISICON[4] and garnet[5] families require high temperature sintering to reduce the effect of grain boundaries to achieve high ionic conductivity, while chalcogenides with malleable lattices can be cold pressed to accomplish high ionic conductivity.

In this respect several sulfide-based solid electrolytes such as thiophosphate (Li_3PS_4),[6] thiostannate (Li_4SnS_4 and Li_2SnS_3),[7,8] thiogermanate (Li_4GeS_4),[9] thioantimonate (Li_3SbS_4)[10] and their aliovalent cationic substituted derivatives, such as $Li_{10}GeP_2S_{12}$[11] and $Li_{4-x}Si_{1-x}P_xS_4$[12,13] have been reported with high room temperature ionic conductivities. Often aliovalent substitution led to new structure type with super-ionic conductivity for example, $Li_{10}GeP_2S_{12}$[11] and many such compositions are now emerging as superionic conductor.[14–16] Notably most of the crystal structures of these ionic conductors are built up of isolated tetrahedral thiometallate building unit with one or two exceptions, such as Li_2SnS_3 which has a layered structure built up of edge-shared SnS_6 octahedra. However, only very few reports are available on selenide-based compounds or anion substitution in sulfide lattice with selenides. Few examples that are available tend to show higher ionic conductivity due to more polarizable nature of selenides compared to sulfides, for example, Li_4SnSe_4 shows a room temperature ionic conductivity of 2 x10^{-2} S cm^{-1}.[17] Therefore, it is crucial to discover new ternary chalcometallate series based on primary tetrahedral building unit in search for new ionic conductors. In this quest we have recently published two new ternary alkali thiogallate phases A_5GaS_4 (*A* = Li and Na) that have similar composition but structurally different on the basis of arrangement of GaS_4 and AS_4 tetrahedra.[18] Intrigued by this discovery, we wanted to further expand the family of ternary phases with basic building unit in the selenide analogue and create more chemical space and scope for the aliovalent substitution. There is an added advantage in discovering tetrahedral chalcometallate unit with triel elements such as Al and Ga as they will crystallize with large number (five) of alkali ions providing opportunities for further defect creation for enhanced ionic conductivity. All of these can be achieved if we first have the basic

[a] *Department of Chemistry, Missouri University of Science and Technology, Rolla, MO 65409, USA.*
[b] *Department of Physics, Missouri University of Science and Technology, Rolla, MO 65409, USA.*
[c] *Department of Chemistry, Missouri State University, Springfield, MO 65897, USA*
†Electronic supplementary information (ESI) available: cif files of the compounds **I**-**IV** (CSD 2204428-2204431). Tables showing atomic coordinates and equivalent isotropic and anisotropic displacement parameters for **I**-**IV**. Figures showing Li-coordination, equivalent circuit for impedance fittings and BVS maps. For ESI and crystallographic data in CIF or other electronic format, See DOI: 10.1039/x0xx00000x

ternary composition with selenide successfully synthesized and crystallographically characterized. Towards this goal, herein, we are reporting for the first time the syntheses, crystal structure, and ionic conductivity of two new ternary selenometallates Li_5MSe_4 (*M* = Al and Ga) that are isostructural to the Li_5GaS_4 phase. Furthermore, we also report the successful substitution of Sn^{4+} for M^{3+} in Li_5MSe_4 to create Li vacancy sites thereby improving the ionic conductivity.

Experimental section

Synthesis

Li_5MSe_4 (*M* = Al (**I**) and Ga (**II**)) was synthesized through high temperature solid-state reaction with stochiometric ratio of 2.5 mmol of Li_2Se, 1 mmol of *M* (Al or Ga), and 1.5 mmol of Se powder taken in a sealed quartz tube. All the chemicals were purchased from Alfa Aesar and Li_2Se was synthesized by stoichiometric mixing elements in liquid ammonia.[19] To create Li-ion vacancy we chose aliovalent doping of 25% Sn^{4+} in M^{3+} site with the removal of equivalent amount of Li^+ for charge balance. To synthesize the targeted composition, $Li_{4.75}M_{0.75}Sn_{0.25}Se_4$, stochiometric amount of Sn (0.25 mmol) and *M* (0.75 mmol) metal powder, Se (1.625 mmol) powder and adjusted amount of Li_2Se (2.375 mmol) were mixed assuming that Sn will be oxidized to +4 oxidation state through the complete reduction of Se to Se^{2-}. However, the obtained compositions after the reactions, $Li_{4.66}Al_{0.82}Sn_{0.22}Se_4$ (**III**) and $Li_{4.37}Ga_{0.89}Sn_{0.24}Se_4$ (**IV**), were slightly off from the targeted composition as explained later. The precursors were loaded in the carbon-coated quartz ampoules inside an Ar-filled glove box (O_2 <0.5 ppm, H_2O <0.5 ppm). The ampoules were brought out from the glove box under air-tight condition and was flame-sealed under vacuum. The sealed ampoules were then kept inside a temperature-programmable furnace and heated to 700 °C at a heating ramp of 20 °C/h and held at that temperature for 48 hours before cooling down to room temperature at 20 °C/h. Dark red chunky crystals for **I** and **II**; dark, and yellow crystals for compounds **III** and **IV**, respectively, were recovered after breaking the ampoules inside the glove box. Suitable crystals were picked for single-crystal X-ray diffraction and well ground powder was used for powder X-ray diffraction and further characterization. The photograph showing the color of the powder samples of **I** – **IV** is given in Figure S1 (ESI).

X-ray Crystallography

Appropriate crystals for **I** – **IV** were chosen under optical microscope for single-crystal X-ray diffraction on a Bruker Smart APEX diffractometer equipped with a sealed-tube X-ray source of Mo-Kα (λ = 0.71073 Å) radiation. It is to be noted here that though as-synthesized product contained large chunks of crystals, it was difficult to get one with single-crystal diffraction quality and only tiny pieces of crystals were suitable for this purpose. Room temperature data sets for **I** – **IV** were collected under dry N_2 stream using SMART[20] software with a step size of 0.3° in ω scan. The program SAINT[21] was used for the data integration and SADABS[21] for absorption correction. The crystal structures were solved from difference Fourier syntheses using SHELXS-97. Full-matrix least-squares refinement against $|F^2|$ was performed using the SHELXTL-PLUS suite of programs.[22] The compounds, **I**-**III**, crystallized in the $P2_1/m$ and compound **IV** in $P\bar{3}m1$ space group. All the atoms were located from the difference Fourier maps and the weighted R factor, wR_2 converged to a lower value with no further unaccounted electron densities. Single-crystal structure solution yielded the intended target composition for **I** and **II**, however, for **III** and **IV** a small amount of Sn was found to substitute one of the lithium sites (Sn2/Li3 in **III** and Sn2/Li1 in **IV**). After refinement of the Li-vacancies, the final charge-balanced compositions, $Li_{4.66}Al_{0.82}Sn_{0.22}Se_4$ (**III**) and $Li_{4.37}Ga_{0.89}Sn_{0.24}Se_4$ (**IV**), deviate slightly from the targeted compositions. The presence of Sn^{4+} has been verified by XPS analysis for the Sn-doped phases, **III** and **IV** (discussed later). Final refinements of anisotropic thermal parameters were carried out using SHELX-2018 incorporated into ShelXLe.[23] Crystal data and the refinement parameters are given in Table 1 and the selected bond lengths are provided in Table 2 for **I** – **IV**. Atomic coordinates and the anisotropic thermal parameters are supplied in the ESI (Tables S1 and S2).

Powder X-ray Diffraction

The laboratory grade powder X-ray diffraction (PXRD) data were collected on a PANalytical X'Pert Pro diffractometer fitted with a Cu Kα anode and a linear array of PIXcel detector over a 2θ range of 5 – 90°. The samples were hand-ground inside the glove box and transferred to an airtight sample holders covered with Kapton film to avoid any contact with the air during the PXRD data collection. The laboratory powder patterns matched well with the simulated patterns generated from the atomic coordinates of single-crystal X-ray structure solution, slight differences in the observed intensities arise from unavoidable preferred orientation (Figures 1, S2, and S3). The lower angle peaks in Li_5MSe_4 are shown in Figure S2. We have also found presence of a minor unknown impurity phase in **I**. Note that, Sn substitution in **I** to create **III** has intensified the formation of same unknown impurity phase (Figure S3) that was also found in **I**. On the other hand, for Sn-doped Li_5GaSe_4, $Li_{4.37}Ga_{0.89}Sn_{0.24}Se_4$ (**IV**), considering 100 % yield of the product with respect to Ga, minor impurity phases consisting of Li_2Se and Li containing tin selenide phases (Li_2SnSe_3 or Li_4SnSe_4) or $SnSe_2$ are expected. These impurities were not detected from the laboratory grade powder X-ray data (compound **IV** in Figure 1).

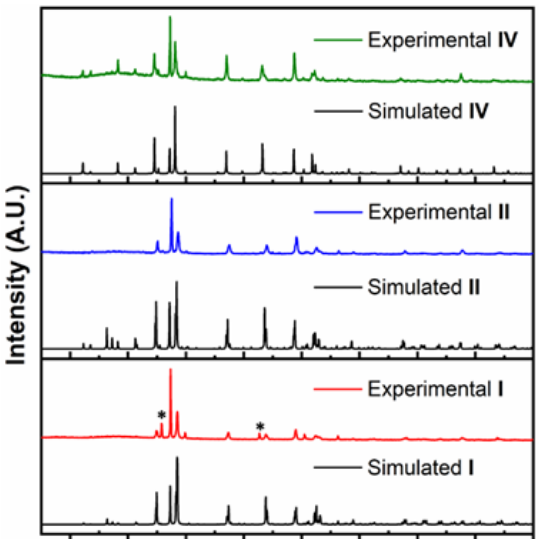

Figure 1. Comparison of laboratory powder X-ray diffraction patterns and simulated patterns of compounds **I**, **II**, and **III**. The asterisk symbol denotes the minor unknown impurity.

Table 1 Crystal Data and Refinement Parameters for compounds, **I** – **IV**.

Compounds	I	II	III	IV
Empirical formula	Li_5AlSe_4	Li_5GaSe_4	$Li_{4.66}Al_{0.82}Sn_{0.22}Se_4$	$Li_{4.37}Ga_{0.89}Sn_{0.24}Se_4$
Formula weight	377.52	420.26	396.42	436.77
Temperature	296(2) K	298(2) K	298(2) K	296(2) K
Wavelength	0.71073 Å	0.71073 Å	0.71073 Å	0.71073
Crystal system	Monoclinic	Monoclinic	Monoclinic	Trigonal
Space group	$P2_1/m$	$P2_1/m$	$P2_1/m$	$P\bar{3}m1$
a/Å	6.5450(3)	6.5565(6)	6.5800(4)	8.3630(3)
b/Å	8.2330(4)	8.2530(2)	8.2800(5)	8.3630(3)
c/Å	7.1840(3)	7.1966(7)	7.2380(4)	6.5530(2)
α (°)	90	90	90	90
β (°)	90.149(6)	90.293(3)	90.134(8)	90
γ (°)	90	90	90	120
Volume/ $Å^3$	387.10(3)	389.39(16)	394.3(4)	396.9(3)
Z	2	2	2	2
Density (calculated)	3.239 Mg/m^3	3.584 Mg/m^3	3.339 Mg/m^3	3.654 Mg/m^3
Absorption coefficient	18.949 mm^{-1}	22.112 mm^{-1}	19.265 mm^{-1}	22.072 mm^{-1}
Goodness-of-fit on F^2	1.138	1.093	1.108	1.137
R1 [$I > 2\sigma(I)$]	R1 = 0.0474	R1 = 0.0364	R1 = 0.0373	R1 = 0.0343
w*R* (*F*2) (all data)	wR2 = 0.1256	wR2 = 0.0961	wR2 = 0.1061	wR2 = 0.0980

[a]R1 = ∑||Fo| − |Fc||/∑|Fo|. [b]wR2 = {∑[w(Fo 2 − Fc 2)2]/ ∑[w(Fo 2)2]}1/2, where w = 1/[σ2 (Fo)2 + (aP)2 + bP], where P = (Fo 2 + 2Fc 2)/3.

Table 2 Selected Bond Lengths (Å) for compounds **I** – **IV.**

M – Se	M = Al	M = Ga	M = Al/Sn		M = Ga/Sn
M1 – Se1	2.3760(3)	2.3994(5)	2.4140(2)	M1 – Se1	2.4598(4)
M1 – Se2	2.3950(3)	2.4176(4)	2.4080(2)	M1 – $Se1^{\#2}$	2.4598(4)
M1 – Se3	2.3854(9)	2.4199(7)	2.4241(4)	M1 – $Se1^{\#3}$	2.4598(5)
M1 – $Se3^{\#1}$	2.3854(9)	2.4199(7)	2.4241(4)	M1 – Se2	2.4600(2)

Thermal Analysis

TGA and DSC experiments on all compounds were carried out simultaneously on SDT Q600 instrument from room temperature to 900 °C at a ramping rate of 10 °C/min under the flow of high purity Argon gas. The samples *ca*. 20 mg mass was quickly transferred within ~10 Sec into alumina crucible and placed with ~5 sec into the instrument balance pan for the analysis. The TGA and DSC plots of all the compounds are presented in Figure S4. All the compounds exhibited an initial weight loss until 100 °C that can be ascribed to the unavoidable water adsorption due to exposure to air while transferring into the instrument or samples' handling upon preparation and packing. Following that, again weight loss was observed after 300 °C for all the samples presumably due to the reaction with the traces of oxygen impurity in Ar purge gas with the surface of the compounds. Due to the constant weight loss, the DSC traces were inconclusive. However, for **IV** an endothermic peak can be seen at 773 °C presumably due to some kind of phase transition (Figure S4d).

X-ray Photoelectron Spectroscopy

X-ray Photoelectron Spectroscopy (XPS) was carried out using Thermo scientific-Nexsa surface analysis spectrometer on compounds **III** and **IV** to verify the doping of Sn^{4+} in Li_5MSe_4. Monochromated Al-Kα source was used to collect the spectrum. High resolution spectra for Al 2*p*, Ga 2*p*, Sn 3*d*, and Se 3*d* were collected with a 400 µm spot size and a pass energy of 50 eV with 0.1 eV energy step. The samples were loaded into a Vacuum Transfer Module (VTM) inside glovebox to avoid exposure to air and transferred into the instrument. All the spectra were calibrated using C 1s peak (285.0 eV) before any further analysis. Figure S5a shows Al 2*p* spectrum centered at 74 eV indicating the presence of Al^{3+} state. The peak splitting in Al 2*p* is ignored owing to narrow spin-orbit splitting energy for Al^{3+} (Δ = 0.44 eV). Figure S5d shows a doublet of Ga $2p_{3/2}$ and $2p_{1/2}$ at 1117.50 and 1144.36 eV attributed to the +3 oxidation state of Ga.[24] Figure S5b and S5e represents the Sn $3d_{5/2}$ and $3d_{3/2}$ doublet located at 486.14 and 494.54 eV confirming the successful doping of Sn^{4+} into Li_5MSe_4.[25] Finally, Se 3*d* spectra (Figure S5c and S5f) with $3d_{5/2}$ and $3d_{3/2}$ at energies 53.39 and 54.32 eV indicate the presence of Se^{2-} state signifying complete reduction of Se to Se^{2-} in both the compounds, **III** and **IV**.[24]

DRS Studies

Diffuse Reflectance Spectroscopy (DRS) measurements on compounds were performed using a praying mantis setup on Varian CARY 5000 UV-Vis-NIR spectrometer. $BaSO_4$ (Fisher, 99.2%) was used as an ~100% reflectance standard. The reflectance data were converted to absorption using Kubelka-Munk function to determine the optical band gap of the compounds.[26] The hν *vs.* $(\alpha h\nu)^2$ plots showed a flat line along the x-axis followed by a steep rise due to the electronic transition from the valence band to the conduction band. The band gap was further determined by the intersection of the extrapolated flat and the first steep rise of the plot (Figure 2). Note that there also exist second absorption shoulder in all the spectra. These second absorption can be attributed to impurity phases in the case of **I** and **III**, while for phases **II** and **IV** they appear due to gap in the band structure at higher energy levels.

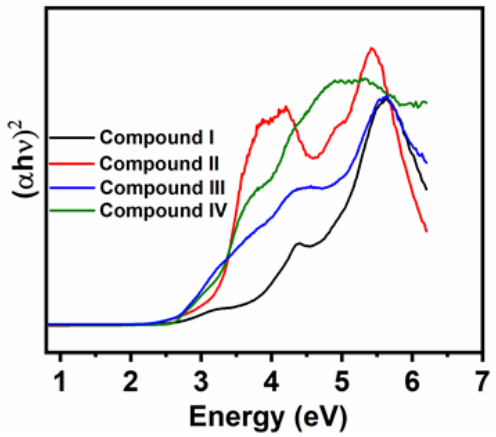

Figure 2. Diffuse reflectance spectra plots of compounds, **I** - **IV.**

AC Impedance measurements

AC Impedance measurements were performed using a Biologic instrument SP-150 impedance analyzer with an AC signal amplitude of 500 mV in the frequency range of 1 Hz to 1 MHz. The hand ground samples were cold pressed with a force of 280 MPa using a stainless-steel pressing die inside an argon filled glovebox (O_2 < 0.1 ppm and H_2O < 0.1 ppm). The pellet was then positioned between the blocking electrodes (indium foils) inside an airtight Swagelok type cell. The cell was placed in a temperature-controlled furnace and heated to measure the temperature dependent ionic conductivity of the compounds. The impedance data were collected for every 10 °C increment in the temperature range starting from room temperature to 75 °C. The temperatures were kept constant at every step for an hour for the cell to reach its thermal equilibrium before the data collection.

DFT calculations

The Density Functional Theory (DFT) calculations were performed using VASP computational package on both compounds to investigate the electronic band structure.[27–30] The revised Perdew–Burke– Ernzerhof generalized gradient approximation (PBESol) was employed to the density functional[31] and Projected Augmented Wave (PAW) pseudopotential were used to describe the effect of the core electrons. The energy cut-off was set to 520 eV for all the calculations and the Brillouin zone integration used Monkhorst-Pack[32] k-point grids with the dimension of 4 x 3 x 3 for both **I** and **II**.

Results and discussion

Structural description

The compounds, **I** – **III**, are isostructural and crystallize in centrosymmetric monoclinic, $P2_1/m$ space group as their sulfide analogues, Li_5GaS_4[18] and Li_5AlS_4.[33] The asymmetric unit (Figure 3a and S6) consists of one main group atom (Al or Ga), four crystallographically distinct lithium and three selenium atoms. In $Li_{4.66}Al_{0.82}Sn_{0.22}Se_4$ (**III**), Sn^{4+} partially substitutes both Al and Li (Li3) in their respective sites. Owing to the aliovalent substitution, vacancies are created in all the Li sites. The main group atom, two lithium atoms (Li2 and Li3), and two selenium (Se1 and Se2) atoms occupy special positions denoted by 2*e* Wyckoff site. One lithium (Li1) and one selenium (Se1) occupy general positions denoted as 4*f* Wyckoff site. The Li4 site also occupies a special position, 2*d* Wyckoff site. The detailed structural description can be found in our previous publication[18] and here we will discuss only the salient features. Li1 and Li3 adopt distorted tetrahedral coordination in the same fashion as the MSe_4 tetrahedra. Li2 and Li4 adopt distorted octahedral coordination (Figures S7a and S7b). The structure can also be described in terms of close packing of anions. Se atoms form a hexagonal closed packing of anions stacked along *a*-axis in ABAB fashion. Such close packed Se anion stacking generates eight tetrahedral (*Td*) and four octahedral (*Oh*) holes based on the four Se in the formula, Li_5MSe_4. Out of the available holes, 3/8th *Td* holes are occupied by Li (Li1 and Li3) and main group atoms (Ga or Al) and ½ of the octahedral holes are filled with Li (Li2 and Li4). The pair of close-packed layers containing the *Td* cations alternate with layers containing the *Oh* Li-ions. Such filling of cations also allows us to imagine the structure as if the *Td* ions containing pair of Se-layers forming a layered honeycomb type lattice structure (Figure 3c) through the edge sharing of MSe_4 and $LiSe_4$ (Li1 and Li3) tetrahedra along the *a*-axis intervened by the *Oh* Li-ions (Li2 and Li4) as shown in Figure 3b. The Li – Se bond distances are in the range, 2.496(2) – 2.689(3) Å, for tetrahedral coordination and 2.700(2) – 3.005(3) Å for octahedral coordination and are in good agreement with Li containing main group selenides such as $LiMSe_2$ (*M* = Al and Ga)[34,35] and Li_4SnSe_4.[17] $Li_{4.37}Ga_{0.89}Sn_{0.24}Se_4$ (**IV**), on the other hand, crystallizes in trigonal $P\bar{3}m1$ space group with two selenium atoms, one gallium atom, and two lithium atoms in the asymmetric unit (Figure 3d). The Sn^{4+} substitutes part of Ga on gallium site and a small percentage in tetrahedrally coordinated lithium site (Li1). The Ga1/Sn1 and Se2 occupy special positions denoted by 2*d* Wyckoff symbol, one of the Li-atoms (Li2) also occupies special position denoted by 3*f* Wyckoff site and all other atoms occupy the 6*i* general positions. The structure can be visualized as a 2-dimensional (2-D) layered structure with edge sharing $(Ga/Sn)Se_4$ and $LiSe_4$ (Li1) distorted tetrahedra. The inter layer spaces are filled with Li (Li2) ions in distorted octahedral coordination with Se (Figure 3e, and Figure S7c). The substituted Sn (Sn1 and Sn2) atoms partially occupy tetrahedrally coordinated Ga1 and Li1 sites, respectively. The structure also forms a close packing of Se atoms along *c*-axis, generating four *Oh* and eight *Td* sites. Here, 1/4th of *Td* sites is occupied by Ga1/Sn1 and Li1/Sn2 atoms and 1/4th of the *Oh* sites are occupied by Li2 atom. Further, the edge sharing *Td* layers of compound **IV** can be envisioned as a honeycomb structure along *c*-

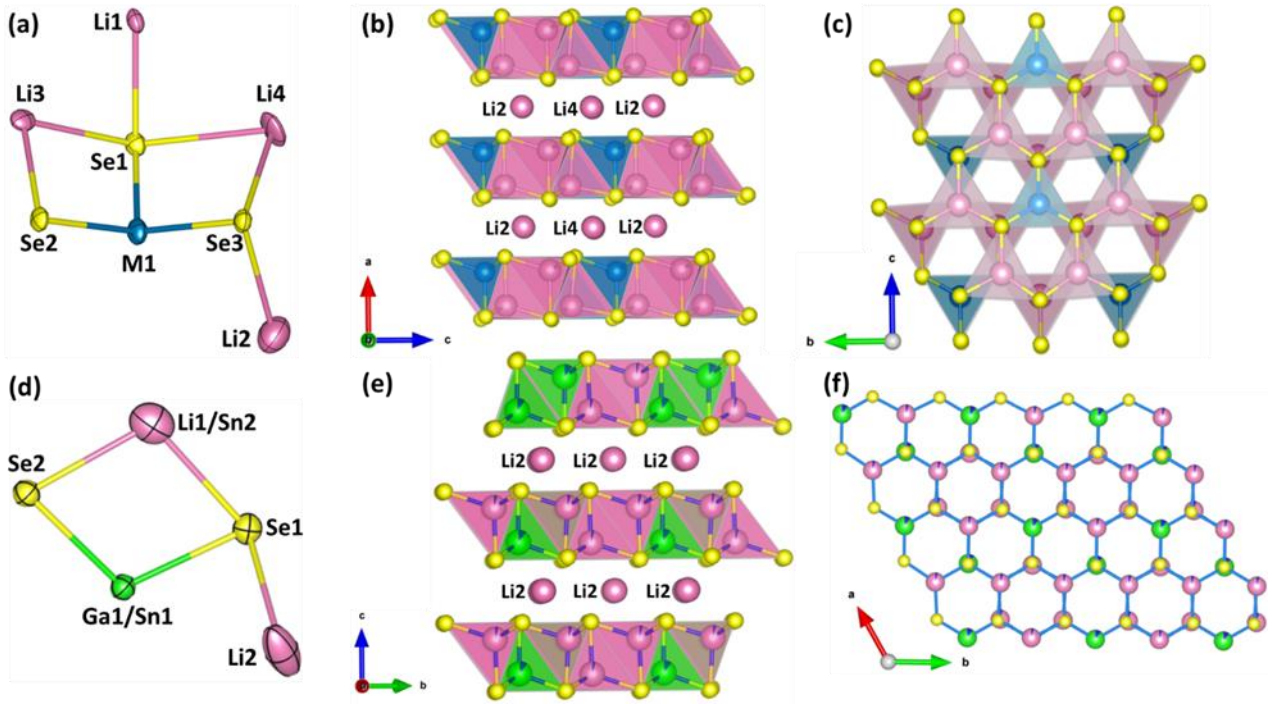

Figure 3. (a) Asymmetric unit of Li_5MSe_4. (b) Pseudo layers formed by edge sharing MSe_4 and $LiSe_4$ tetrahedra along *a*-axis with the inter layers filled with octahedrally coordinated Li atoms. (c) polyhedral view from *a*-axis showing the 3/8th occupancy of *Td* holes by *M* and Li atoms. (d) Asymmetric unit of $Li_{4.37}Ga_{0.89}Sn_{0.24}Se_4$ (**IV**). (e) Layer formation by Ga/SnSe4 and Li/SnSe4 tetrahedra with octahedral Li in the interlayers. (f) Honeycomb ordering in **IV** along *c*-axis.

axis as shown in Figure 3f. The Sn/Ga – Se bond distances are in the range, 2.459(4) – 2.460(2) Å are well within the expected range as they lie in between pure Ga – Se and Sn – Se (Li_4SnSe_4)[17] distances in tetrahedral coordination (also see Table 2). It is also important to note that owing to the substitution of heavy atom such as Sn in the *Td* Li-site, Sn-substituted Li_5GaSe_4 crystallizes in a higher symmetry crystal system, however, such phase transition did not occur in the Sn-substituted Li_5AlSe_4. A deeper insight reveals that that $P\bar{3}m1$ and $P2_1/m$ are related through maximal group-subgroup pair ($P\bar{3}m1$>$P2_1/m$) through an intermediate subgroup, *C*2/*m*, following Bärnighausen's convention.[36] The chain of maximal subgroups with an overall index of 6 can reduce $P\bar{3}m1$ to subgroups following their corresponding indices as shown below $\mathbf{P\bar{3}m1\ (164)} \xrightarrow{t3} \mathbf{C2/m\ (12)} \xrightarrow{k2} \mathbf{P2_1/m\ (11)}$.[37,38] According to the group-subgroup relationship $P\bar{3}m1$ (164) and *C*2/*m* (12) are related through t-subgroup (translationengleiche subgroup I) with an index of 3 and *C*2/*m* (12)>$P2_1/m$ (11) are related to k-subgroup (klassengleiche subgroup IIa) with an index of 2. The overall index 6 (3 x 2 = 6) can be generated from the product of the indices of the group-subgroup pairs forming the group-subgroup chain. Through the group-subgroup relationship the cell parameters can be transformed keeping *b*-axis unique and the 2*d* and 6*i* Wyckoff positions in $P\bar{3}m1$ split into two 2*e* and one 4*f* positions for anion (Se) in $P2_1/m$. Generally, ionic radius of the dopant ion (Sn^{4+}) is a determining factor while considering which cation will be replaced by the dopant ion. In these cases, both Al^{3+} (0.39 Å) and Ga^{3+} (0.47 Å) ionic radii are ~29 and 14.5 % smaller than Sn^{4+} (0.55 Å), respectively. However, the differences in ionic radii are much less when Sn^{4+} is compared with the ionic radii of Li^+ [0.59 Å (Td) and 0.76 Å (Oh)], which are ~7 and ~10% greater than the Sn^{4+} for Td and Oh coordination, respectively. Therefore, there is no surprise that Sn^{4+} also replaces part of the Li^+ besides replacing the triel ions. It turns out that doping of Sn^{4+} in Li_5GaSe_4 reduces the distortion of tetrahedral Ga and Li site substantially as evident from the distortion index of Ga/$SnSe_4$ and $LiSe_4$ (Table S3),[39] resulting in a phase transition to a higher symmetry space group. While such Sn^{4+} substitution does not reduce the distortion of the Al *Td* or *Oh* Li site as the difference between the ionic radii of Al^{3+} and Sn^{4+} is much higher. Thermal analysis (simultaneous TG-DSC) was carried out to evaluate whether any of the lower symmetry monoclinic phases transition to higher symmetry trigonal phase or *vice versa*. These experiments were not very conclusive because of the weight loss events masking the true thermal events (Figure S4). However, in the case of **IV**, an endothermic peak is clearly observed at 773 °C, which may signify a phase transition from trigonal to monoclinic (Figure S4d). However, further experimental verification such as *in situ* thermodiffractogram is required to confirm such phase transition.

Theoretical Calculations

From the elucidated structures of **I** and **II**, structural relaxations were performed until the maximum force on the atoms came down to less than 10^{-2} eV $Å^{-1}$. The relaxed structures converged well with the experimental solutions. The theoretical volumes obtained from the relaxed structures are ~6 and ~9 $Å^3$ smaller than the experimental one. The theoretical band gaps obtained from DFT calculations, 2.83 and 2.05 eV (Figures 4a and 4b), are lower than the experimental band gaps obtained from the DRS measurements, 3.65 and 3.2 eV, for **I** and **II**, respectively (Figure 2). The underestimation of the band gap by DFT is well-known and often it has to do with the inaccurate approximation of the exchange–correlation potential energy term.

The band gap of Ga-analogue is lower than the Al-analogue owing to the increased covalency between Ga – Se than the Al – Se bond. Figures 4a and 4b show the projected density of states for **I** and **II**, respectively. In both cases the valence band near the Fermi level is dominated by the Se 4*p* states. The conduction band minimum, on the other hand, has major contribution from *M* n*s* states (Al 3*s* states or Ga 4*s* states) admixed with Se 4*p* states. Hence, the optical band gap measurements can be assigned for the electronic transitions from Se 4*p* orbitals to most-likely anti-bonding orbitals formed by *M* n*s* and Se 4*p* orbitals. The minimal contribution from the Li 1*s* state in the valence band indicates that the interaction between Li and Se is predominantly ionic. Note that aliovalent substitution of Sn in Li_5MSe_4 narrows the band gap as it is evident from the DRS spectra and by the change in color of the powdered samples from brownish-grey to mocha and from beige to mustard for **III** and **IV**, respectively (Figure S1). The cause of band gap narrowing is most likely due to the participation of 5*s* orbital of Sn in lowering the bottom of the conduction band.

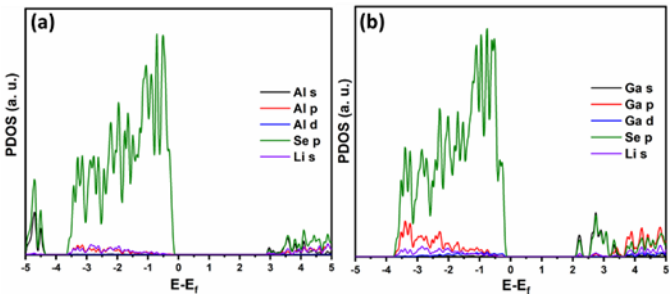

Figure 4. Projected electronic density of states of (a) Li_5AlSe_4 (**I**) and (b) Li_5GaSe_4 (**II**).

Ionic conductivity

AC impedance measurements were conducted on **I** – **IV** to determine the ionic conductivity and activation energies. The impedance spectra are plotted in the form of Nyquist plot with a semi-circle at higher frequency range followed by a tail at the low frequencies attributed to the bulk resistance and charge accumulation at the blocking electrodes, respectively. The room temperature ionic conductivity is derived from the bulk resistance obtained from the Nyquist plot through fitting using equivalent electrical circuits given in the ESI (Figure S8). The temperature dependent ionic conductivities were measured for **I** and **II** from room temperature to 75 °C at an interval of 10 °C between each measurement (Figures 5a and 5b). Since ionic conductivity of **I** and **II** follows Arrhenius behaviour, the activation energies (E_a) are calculated using the equation, $\sigma_T = \sigma_o \exp(-E_a/k_BT)$ where, σ_T is the ionic conductivity at a given temperature (T), σ_o is a pre-exponential factor, k_B is the Boltzmann constant, and T is the absolute temperature. A room temperature ionic conductivity of 0.60 x 10^{-7} and 0.58 x 10^{-7} S cm^{-1} are obtained with calculated activation energies of 0.51 and 0.48 eV for **I** and **II**, respectively.

As both the compounds are structurally identical, the ionic conductivity and activation energies are also in the same range for **I** and **II**. To further examine the low ionic conductivity of these ternary selenometallates, we performed Bond Valence Energy Landscape (BVEL) calculations to identify the minimum energy barrier path for the percolation of Li^+ ions. A well-connected bond valence sum map within the lattice can be correlated to the plausible Li^+ ion conduction path within the structure. These paths are plotted as an isosurface ($|\Delta V|$) for better visualization using VESTA software.[40] The BVEL maps plotted at different $|\Delta V|$ = 0.3, 0.5, and 0.8 v.u. for both **I** and **II** show no conceivable percolation path for the Li^+ ions which attributes to their low ionic conductivities (Figures S9 in ESI). However, the ionic conductivity of Li_5AlSe_4 is slightly higher than its isostructural sulfide counterpart, Li_5AlS_4 (σ_T = 9.73 x 10^{-9} S cm^{-1}).[33] On the other hand, the ionic conductivity Li_5GaSe_4 is almost identical to its sulfide analogue, Li_5GaS_4 (σ_T = 1.80 x 10^{-7} S cm^{-1}).[18] The ionic conductivities are lower than other ternary selenometallates such as Li_4SnSe_4 (σ_T = 2 x 10^{-5} S cm^{-1}).[17] There are numerous reports on the aliovalent cation substitution (M = Al^{3+}, Sn^{4+}, or P^{5+}) in main group ternary sulfide phases to create vacancies in the Li sites thereby boosting the ionic conductivity.[15,16,41,42] Interestingly, only few ternary selenide phases are known so far and investigation of substitutional chemistry to find better ionic conductors have been limited.[43–46] Therefore, synthesis and structural characterization of Li-selenometallates of triel elements gives us an opportunity to perform aliovalent substitution to increase the ionic-conductivity. We, therefore, substituted Sn^{4+} in the *M*-site of Li_5MSe_4 thereby creating vacancies in Li site and observed substantial improvements in ionic conductivity. The doped compositions, $Li_{4.66}Al_{0.82}Sn_{0.22}Se_4$ (**III**) and $Li_{4.37}Ga_{0.89}Sn_{0.24}Se_4$ (**IV**), show five-fold increase in ionic conductivity, 3.37 x 10^{-7} S cm^{-1} and 2.4 x 10^{-7} S cm^{-1}, (Figure 5c and 5d) with activation energies of 0.52 and 0.28 eV, respectively. In both cases, Sn^{4+} substitutes M^{3+} and Li^+ sites of Li_5MSe_4. This aliovalent substitution increased the ionic conductivity of both **III** and **IV**. However, **III** has vacancies in both *Td* (Li1) and *Oh* (Li2 and Li4) sites of Li^+ and in case of **IV** no such vacancies were observed in *Oh* (Li2) site. BVEL calculations at high $|\Delta V|$ values show a plausible Li^+ conduction path in **III** through *Td* and *Oh* sites of Li^+ ions whereas in **IV** conduction path is discerned only through fully occupied *Oh* site resulting in slightly lower ionic conductivity than **III** (Figure S10).

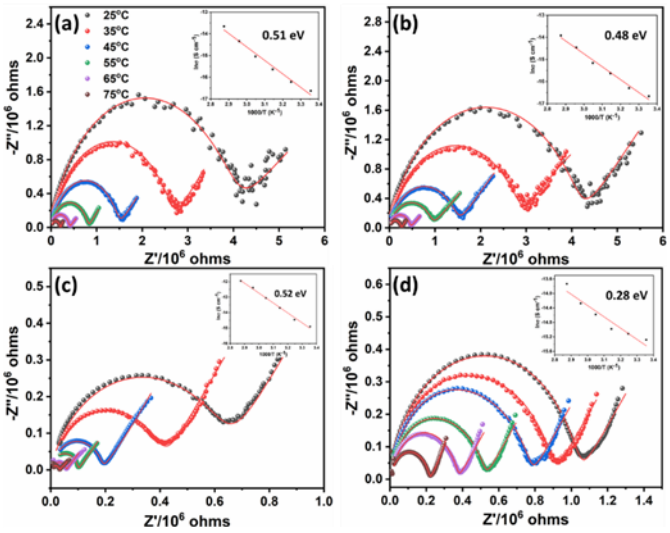

Figure 5. Nyquist plot from the AC impedance spectroscopy of (a) compound **I** (Li_5AlSe_4), (b) compound **II** (Li_5GaSe_4), (c) compound **III** ($Li_{4.66}Al_{0.82}Sn_{0.22}Se_4$) (d) compound **IV**($Li_{4.37}Ga_{0.89}Sn_{0.24}Se_4$). Insets in the figure shows the calculated activation energies for each compound using Arrhenius equation.

Further improvement of ionic conductivity is most likely impeded due to presence of Sn in Td Li-site. However, additional optimization is required both in terms pure phase synthesis and substituting other aliovalent main group elements. It is also imperative to contemplate that the pseudo 2-D structure of Li_5MSe_4 offers an opportunity to substitute part of the *Td* Li with suitable transition metal and create redox active chalcogenide lattice which can act as cathodes for Li-ion batteries and display dual cationic and anionic redox behaviour.

Conclusion

Two new ternary selenometallates, Li_5MSe_4 (*M* = Al and Ga), have been successfully synthesized through high temperature solid-state synthesis. The crystal structure solution through single-crystal X-ray diffraction revealed a pseudo 2-D layer type structure for both compositions with optical band gap in the range of ~3.5 eV. AC impedance spectroscopy along with BVEL maps suggest no possible percolation path for the Li^+ ions. Aliovalent substitution of Sn^{4+} in M^{3+} site shows five-fold improved ionic conductivity. DFT calculations show majority of the valence band is constructed from Se 4*p*-states and no significant contribution from Li-orbitals indicate ionic interaction between Li and Se. These new ternary phases can act as a parent structure to perform various aliovalent substitutions in the triel site as well as halogen substitution in the selenium site in search for better chalcogenide cathodes and ionic conductors.

Author Contributions

AC conceived the problem and supervised the work. SS carried out the synthesis, characterization, and property measurements. SS also performed band structure calculation under the supervision of AVC. NG helped with the TG-DSC study. SS and AC wrote the manuscript, and all the authors approved the manuscript and gave feedback.

Conflicts of interest

There are no conflicts to declare.

Acknowledgements

The authors acknowledge the funding from the National Science Foundation (DMR-1809128).

References

1 Z. Zhang, Y. Shao, B. Lotsch, Y. S. Hu, H. Li, J. Janek, L. F. Nazar, C. W. Nan, J. Maier, M. Armand and L. Chen, *Energy Environ. Sci.*, 2018, **11**, 1945–1976.
2 J. Janek and W. G. Zeier, *Nat. Energy*, 2016, **1**, 1–4.
3 K. B. Hueso, M. Armand and T. Rojo, *Energy Environ. Sci.*, 2013, **6**, 734–749.
4 H. Y. P. Hong, *Mater. Res. Bull.*, 1978, **13**, 117–124.
5 V. Thangadurai, H. Kaack and W. J. F. Weppner, *J. Am. Ceramic Soc.*, 2003, **86**, 437–440.
6 Z. Liu, W. Fu, E. A. Payzant, X. Yu, Z. Wu, N. J. Dudney, J. Kiggans, K. Hong, A. J. Rondinone and C. Liang, *J. Am. Chem. Soc.*, 2013, **135**, 975–978.
7 T. Kaib, S. Haddadpour, M. Kapitein, P. Bron, C. Schröder, H. Eckert, B. Roling and S. Dehnen, *Chem. Mater.*, 2012, **24**, 2211–2219.
8 J. A. Brant, D. M. Massi, N. A. W. Holzwarth, J. H. Macneil, A. P. Douvalis, T. Bakas, S. W. Martin, M. D. Gross and J. A. Aitken, *Chem. Mater.*, 2015, **27**, 189–196.
9 R. Kanno, T. Hata, Y. Kawamoto and M. Irie, *Solid State Ion.*, 2000, **130**, 97–104.
10 T. Kimura, A. Kato, C. Hotehama, A. Sakuda, A. Hayashi and M. Tatsumisago, *Solid State Ion.*, 2019, **333**, 45–49.
11 N. Kamaya, K. Homma, Y. Yamakawa, M. Hirayama, R. Kanno, M. Yonemura, T. Kamiyama, Y. Kato, S. Hama, K. Kawamoto and A. Mitsui, *Nat. Mater.*, 2011, **10**, 682–686.
12 M. Murayama, R. Kanno, M. Irie, S. Ito, T. Hata, N. Sonoyama and Y. Kawamoto, *J Solid State Chem.*, 2002, **168**, 140–148.
13 L. Zhou, A. Assoud, A. Shyamsunder, A. Huq, Q. Zhang, P. Hartmann, J. Kulisch and L. F. Nazar, *Chem. Mater.*, 2019, **31**, 7801–7811.
14 P. Bron, S. Johansson, K. Zick, J. Schmedt auf der Günne, S. Dehnen and B. Roling, *J. Am. Chem. Soc.*, 2013, **135**, 15694–15697.
15 P. Bron, S. Dehnen and B. Roling, *J. Power Sources*, 2016, **329**, 530–535.
16 T. Krauskopf, S. P. Culver and W. G. Zeier, *Chem Mater.*, 2018, **30**, 1791–1798.
17 T. Kaib, P. Bron, S. Haddadpour, L. Mayrhofer, L. Pastewka, T. T. Järvi, M. Moseler, B. Roling and S. Dehnen, *Chem. Mater.*, 2013, **25**, 2961–2969.
18 S. Balijapelly, P. Sandineni, A. Adhikary, N. N. Gerasimchuk, A. v. Chernatynskiy and A. Choudhury, *Dalton Trans.*, 2021, **50**, 7372–7379.
19 I.Schewe-Miller, Metallreiche Hauptgruppenmetall - Chalkogenverbindungen: Synthese, Struckturen und Eigenschaften. Ph.D. Thesis, Universität Stuttgart, 1990.
20 *Bruker- SMART*, Bruker AXS Inc., Madison, Wisconsin, USA, 2002.
21 *Bruker- SAINT* and *SADABS*, and *SHELXTL*, Bruker AXS Inc., Madison, Wisconsin, USA, 2008.
22 G. M. Sheldrick, *Acta Crystallogr. A*, 2008, **64**, 112–122.
23 C. B. Hübschle, G. M. Sheldrick and B. Dittrich, *J. Appl. Crystallogr.*, 2011, **44**, 1281–1284.
24 A. A. Lavrentyev, B. v. Gabrelian, V. T. Vu, L. N. Ananchenko, L. I. Isaenko, A. P. Yelisseyev and O. Y. Khyzhun, *Opt. Mater. (Amst)*, 2017, **66**, 149–159.
25 A. Sierra-Castillo, E. Haye, S. Acosta, R. Arenal, C. Bittencourt and J. F. Colomer, *RSC Adv.*, 2021, **11**, 36483–36493.
26 P. Kubelka and F. Munk, *Z. Techn. Phys.,* 1931, 593–601.
27 G. Kresse and J. Hafner, *Phys. Rev. B*, 1993, **47**, 558–561.
28 G. Kresse and J. Furthmüller, *Comput. Mater. Sci.*, 1996, **6**, 15–50.
29 G. Kresse and J. Furthmüller, *Phys. Rev. B*, 1996, **54**, 11169–11186.
30 G. Kresse and D. Joubert, *Phys. Rev. B*, 1999, **59**, 1758–1775.

31 J. P. Perdew, A. Ruzsinszky, G. I. Csonka, O. A. Vydrov, G. E. Scuseria, L. A. Constantin, X. Zhou and K. Burke, *Phys. Rev. Lett.*, 2008, **100**, 136406.

32 H. J. Monkhorst and J. D. Pack, *Phys. Rev. B*, 1976, **13**, 5188–5192.

33 H. Lim, S. C. Kim, J. Kim, Y. il Kim and S. J. Kim, *J. Solid State Chem.*, 2018, **257**, 19–25.

34 J. Kim and T. Hughbanks, *Inorg. Chem.*, 2000, **39**, 3092–3097.

35 K. Kuriyama and T. Nozaki, *J. Appl. Phys.*, 1981, **52**, 6441–6443.

36 H. Bärnighausen, *MATCH, Commun. Math. Comput. Chem.*, 1980, **9**, 139–175.

37 M. I. Aroyo, J. M. Perez-Mato, C. Capillas, E. Kroumova, S. Ivantchev, G. Madariaga, A. Kirov and H. Wondratschek, *Z Kristallogr. Cryst. Mater.*, 2006, **221**, 15–27.

38 M. I. Aroyo, A. Kirov, C. Capillas, J. M. Perez-Mato and H. Wondratschek, *Acta Crystallogr. A*, 2006, **62**, 115–128.

39 W. H. Baur, *Acta Crystallogr. B*, 1974, **30**, 1195–1215.

40 K. Momma and F. Izumi, *J. Appl. Crystallogr.*, 2011, **44**, 1272–1276.

41 P. Zhou, J. Wang, F. Cheng, F. Li and J. Chen, *Chem. Comm.*, 2016, **52**, 6091–6094.

42 J. Lau, R. H. DeBlock, D. M. Butts, D. S. Ashby, C. S. Choi and B. S. Dunn, *Adv. Energy Mater.*, 2018, **8**, 1800933.

43 Z. Liu, Y. Tang, Y. Wang and F. Huang, *J. Power Sources*, 2014, **260**, 264–267.

44 K. Yang, J. Dong, L. Zhang, Y. Li and L. Wang, *J. Am. Ceramic Soc.*, 2015, **98**, 3831–3835.

45 M. A. T. Marple, B. G. Aitken, S. Kim and S. Sen, *Chem. Mater.*, 2018, **30**, 5896–5903.

46 B. T. Leube, K. K. Inglis, E. J. Carrington, P. M. Sharp, J. F. Shin, A. R. Neale, T. D. Manning, M. J. Pitcher, L. J. Hardwick, M. S. Dyer, F. Blanc, J. B. Claridge and M. J. Rosseinsky, *Chem. Mater.*, 2018, **30**, 7183–7200.